ADVANCED MATERIALS INTERFACES
Open Access
www.advmatinterfaces.de

Interface-Controlled Biomimetic Intrafibrillar Mineralization of Collagen: Effect of $Ca^{2+}/[PO_4]^{3-}$ Concentration Ratio

*Urasawadee Amornkitbamrung, Yongjae In, Jung Heon Lee, Zhen Wang, Sang Ho Oh, Heungsoo Shin, Dae Sung Yoon, and Hyunjung Shin**

Mineralized fibrils are important building blocks in bone tissue, formed by the hierarchical assembly of collagen molecules and crystalline hydroxyapatite (HAp). The mineralization pathway of HAp is reported as a nonclassical-crystallization, but the nanoconfined crystallization in collagen fibrils remains poorly understood. The mechanism of intrafibrillar mineralization of collagen-PDA fibrils in modified-simulated body fluid (m-SBF) solution is studied. Collagen-amorphous calcium phosphate (ACP) fibrils are obtained by assembling collagen-PDA fibrils with polyaspartic acid (pAsp) as a stabilizer. The ACP undergoes a phase transformation to HAp within the fibrils upon adjusting the phosphate concentration. It is found that the phase transformation of ACP to HAp in collagen fibrils can be accelerated with a 12 h incubation with 1/10 ratio of Ca^{2+} to $[PO_4]^{3-}$. A lower ratio of 1/1 and 1/5 results in a much slower phase transformation. This finding suggests that an elevated concentration of $[PO_4]^{3-}$ is crucial for faster phase transformation. The relationship between the crystallization rate of HAp in the fibrils and the degree of mineralization is found to be linear in all cases, indicating an interface-controlled process. This gives a better understanding of the mechanism of HAp mineralization in collagen fibrils, providing an effective approach to material design.

1. Introduction

An extracellular matrix (ECM) is an intricate network of extracellular molecules secreted by cells. ECMs act not only as a supporting structure for cells to reside and facilitate cellular growth, but also serve as a substrate for cell signaling that defines cellular behaviors and tissue functions.[1–3] Collagen (Col) is one of the main components of ECMs, especially type I collagen (Col-I), which is the most abundant in human and animal bodies. It has become one of the most attractive materials for tissue engineering to fabricate scaffolds due to its high biocompatibility and bioactivity. However, using pure Col alone would limit its applications. For example, it could not satisfy requirements for bone tissue engineering due to its insufficient osteoinductive and osteogenic properties, poor mechanical strength, and lack of structural stability.[4–6] For decades, researchers have found that the excellent mechanical properties of natural bone tissues are related to a special hierarchical structure that is created by intrafibrillar mineralization of collagen.[7–10] Considering the composition of bone tissues, Col and hydroxyapatite (HAp) were intensively used to fabricate tissue engineering scaffolds, which performed well in bone repair.[11,12] HAp is one of the most common forms of calcium phosphate. It has a

U. Amornkitbamrung, Y. In, H. Shin
Nature Inspired Materials Processing Research Center
Sungkyunkwan University
Suwon 16419, South Korea
E-mail: hshin@skku.edu

U. Amornkitbamrung, Y. In, H. Shin
Department of Energy Science
Sungkyunkwan University
Suwon 16419, South Korea

J. H. Lee
School of Advanced Materials Science and Engineering
Sungkyunkwan University
Suwon 16419, South Korea

Z. Wang, S. H. Oh
Department of Energy Engineering
KENTECH Institute for Energy Materials and Devices
Korea Institute of Energy Technology (KENTECH)
Naju 58330, South Korea

H. Shin
Department of Bioengineering
Hanyang University
Seoul 04763, South Korea

D. S. Yoon
Department of Biomedical Engineering
Korea University
Seoul 02841, South Korea

H. Shin
SKKU Institute of Energy Science and Technology (SIEST)
Sungkyunkwan University
Suwon 16419, South Korea

The ORCID identification number(s) for the author(s) of this article can be found under https://doi.org/10.1002/admi.202300384

DOI: 10.1002/admi.202300384

stoichiometric Ca/P ratio of 1.67.[13] With pure HAp, the scaffold shows good properties in terms of strength and hardness, but has inadequate toughness.[12,14] A hybrid strategy using inorganic bioactive materials has been introduced as an alternative way to improve its properties. Among inorganic bioactive materials, HAp has been widely studied as an organic–inorganic hybrid biomaterial since it is a principal inorganic constituent of hard biological tissues. Its intrinsic biocompatibility, bioactivity, mechanical and thermal stabilities, and convenience for surface modification make HAp an excellent material for use in biomedical applications. Intrafibrillar mineralization is a method to generate organic–inorganic composite materials formed from collagen molecules and nano-calcium phosphate minerals.[12,13,15–17]

In simulated body fluid (SBF) at body temperature, 37 °C, HAp formation occurs through nucleation and crystallization preferentially within the gap regions of Col fibrils.[18] Many attempts have been made to mineralized collagen fibrils by understanding the process of biomimetic bone mineralization.[19] Understanding the principles and processes of collagen mineralization in vivo is crucial for developing synthetic procedures to fabricate bone-like Col-HAp composite materials. The principle of Col mineralization is based on interaction between Col and minerals, such as Ca^{2+} and $[PO_4]^{3-}$ ions, that act in extrafibrillar and intrafibrillar mineralization.[20] Extrafibrillar mineralization refers to deposition of minerals only outside of fibrils, while the intrafibrillar mineralization occurs when HAp starts to form in the gap region of Col and grows along the *c*-axis-oriented crystallites.[21,22] In vivo, Col as an ECM can provide a template for mineralization and the process is mediated by various proteins and enzymes, including alkaline phosphatase, osteopontin, and bone sialoprotein.[23–25] Intrafibrillar mineralization of collagen is initiated by negatively charged phosphorylated noncollagenous protein (NCP) and dentin phosphoryn. The proteins enhance local supersaturation to induce the formation of nuclei by attracting Ca^{2+} and PO_4^{3-} via charged amino acids.[26] In vitro, intrafibrillar mineralization has been successfully achieved using acidic polymers (e.g., polyaspatic (pAsp) and polyacrlic acids as biomimetic analogs) bound with ions, inhibiting other types of nucleation.[27–29] The polymers play an essential role in collagen intrafibrillar mineralization by forming a precursor, often called a polymer-induced liquid-phase precursor (PILP), and collecting ions. In the liquid phase, PILP can be delivered to certain areas in the fibrils via electrostatic interactions.[18] PILP is a transient state in nonclassical crystallization. Recent studies have focused on understanding the mechanisms of Col intrafibrillar mineralization to control and manipulate the process.[17] Solution chemistry involving amorphous calcium phosphate (ACP) has often been reported. The initial molar ratio of Ca^{2+} to PO_4^{3-} in solution affects the structure of ACP formed and subsequently the crystallization of HAp. The Ca–P bonding geometry varies from monodentate to mixed monodentate with bidentate to bidentate as the $Ca^{2+}/[PO_4]^{3-}$ ratio increases from 1/5 to 5/1. The monodentate materials transform directly to HAp, while the bidentate material forms brushite.[30,31] For intrafibrillar mineralization, it has been hypothesized that the phenomenon of size exclusion is important, where molecules larger than 40 kDa are excluded from the fibrils. This happens by inhibiting mineralization everywhere but inside the fibrils, allowing Ca and P to infiltrate, resulting in an initial formation of HAp within the gap zones of the fibrils.[32–34] The process of Col self-assembly can be influenced by the presence of pAsp, which induces the formation of PILP. The pAsp has a strong binding affinity for Ca ions, resulting in complexation, which has been used for targeting bone tissue and promoting biomineralization.[32,35] This PILP process generates an amorphous liquid-phase mineral precursor to HAp that facilitates intrafibrillar mineralization of type-I Col by affecting negatively charged NCPs or with the presence of negatively charged polymer complexes to the a-band (positively charged) region of Col fibrils.[36–39] Additionally, the fluid characteristics of PILP enables it to be drawn into the nanoscopic gaps and grooves of Col fibrils by capillary action.[20]

In this study, the effects of varying concentration ratios of calcium/phosphate ($Ca^{2+}/[PO_4]^{3-}$) in a modified-SBF (m-SBF) solution on the mineralization rate of collagen-polydopamine (Col-PDA) fibrils were studied. Neutrally charged pAsp complexes were formed at the initial stage of mineralization. The complexes increased in size and became negatively charged with increased mineralization time due to the recruitment of P ions by Ca-rich regions through electrostatic attraction, as schematically illustrated in **Figure 1**a. A Ca-complex inducing biomimetic mineralization phenomenon was recently reported that involves a polyelectrolyte Ca complex as a precursor.[40] ACP is formed and slowly crystallizes over time inside the confined space of the gap region of fibrils, as shown in Figure 1b. This is confirmed by transmission electron microscope (TEM) analysis from each stage of crystallization along with selected area electron diffraction (SAED) patterns, shown in Figure 1c and presented below in detail. The findings suggest that an elevated concentration of $[PO_4]^{3-}$ is crucial to initiating phase transformation of ACP to HAp. With an optimized concentration ratio of $Ca^{2+}/[PO_4]^{3-}$ in the m-SBF solution, the rate of mineralization can be dramatically accelerated. A liquid-like pAsp-complex with Ca and P infiltrated to fibrils then gradually crystallizes to HAp. $Ca^{2+}/[PO_4]^{3-}$ concentration ratios of 1/15 and 1/20 resulted in significantly faster intrafibrillar mineralization. The resulting degree of mineralization showed a linear relationship with HAp nucleation and the growth kinetics during intrafibrillar mineralization, indicating an interface-controlled process.

2. Results and Discussion

2.1. Col-PDA Intrafibrillar Mineralization

Self-assembly of Col-PDA fibrils was done in SBF solution in the presence of NCP, in this study, pAsp and PDA at 37 °C.[21,41] In the Col self-assembly process, the ratio of Col-I to PDA was optimized in our previous study, where the polymerization of dopamine molecules did not affect the Col fibrillar structure.[21] The self-assembled Col-PDA fibrils indicate successful formation with a confirmed band gap of ≈67 nm that was clearly observed in the atomic force microscope image in Figure S1a in the Supporting Information. Col-PDA was also investigated using Fourier transform infrared (FTIR) spectra showing the interaction between PDA and Col-I (Figure S1b, Supporting Information). The spectra showed the absorption bands of amide A with N–H stretching, amide B with CH_2^-, CH_3^-, and C–H asymmetric stretching as polypeptide and protein units in self-assembled Col-I at 3500 and 2946 cm^{-1}. For the amide I–III

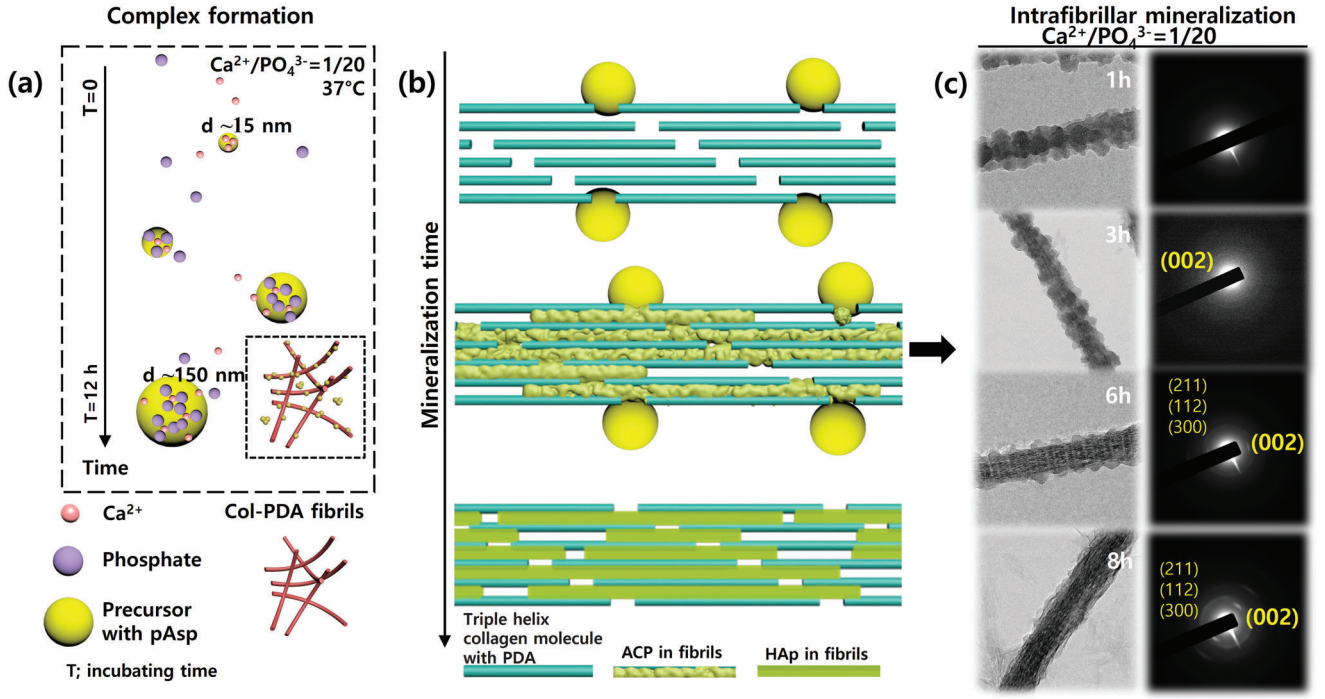

Figure 1. Schematic of intrafibrillar mineralization with precursor-pAsp assistance. a) Precursor-pAsp consisting of Ca and P ions ($Ca^{2+}/[PO_4]^{3-}$ at a concentration ratio of 1/20) in m-SBF evolved into aggregates from ≈15 to 150 nm in diameter over 12 h of incubation. b) pAsp complexes attach to fibrils, infiltrating Ca and P ions in the fibrils leading to crystallization of HAp in the confined space gap region. c) TEM images show precursors attached to fibrils (upper panel), while the middle panel shows crystallization after ions infiltrate into fibrils allowing HAp formation. The corresponding SAED patterns are also shown. The TEM image at the bottom panel shows needle-shape HAp crystals along the *c*-axis oriented parallel to the direction of fibrils. The corresponding SAED pattern is also presented.

bands, peaks were obtained at 1630 (1690–1650 cm^{-1}) from C=O stretching vibrations, amide II at 1542 (1575–1480 cm^{-1}) bands from N–H bending and C–N stretching, and amide III at 1234 cm^{-1}. These results confirm that the native structure of the Col-I molecule is not disrupted after incorporation of PDA.[42–45] The Col-PDA fibrils had a diameter of less than 1 μm, as expected, and were clearly observed using TEM, as shown in **Figure 2**. With no pAsp, small particles ≈20–40 nm in diameter were randomly attached on fibrils, as shown in Figure 2a,b. The particles accumulated into globs of a precursor phase and were also found as nodules, marked with yellow arrows along the fibrils in the high-magnification image of Figure 2b. Calcium phosphate (CaP) phase aggregates are often found and reported as inhomogeneities.[32] These prenucleation species are composed of highly dynamic nanometric ionic clusters that spontaneously form in solution and act as precursors in the HAp crystallization process.[32,46,47] In the presence of pAsp, in Figure 2c,d, low-magnification TEM image shows many particles attached to fibrils creating darker contrast. Furthermore, adsorption of particles in the fibrils allows infiltration of a precursor phase spreading out along the fibrils, as shown in Figure 2d. In both cases, with and without pAsp, an amorphous phase was confirmed in the SAED patterns in the insets of Figure 2b,d, respectively. pAsp acts as a stabilizer, commonly known as a PILP process. Phase separation takes place as ion-sequestered droplets are stabilized in a hydrated amorphous form by an anionic polymer, pAsp, in the current work. The stabilizer inhibits precipitation from solution allowing time for diffusion, enabling infiltration into the fibrils. It is evident that the pronounced banding patterns with infiltration of electron-dense mineral precursors at specific locations are clearly shown in the high-magnification image in Figure 2d, marked with red arrows.

pAsp binds with Ca ions in solution, forming a mineral complex with high levels of Ca ions. Particle size measurements were done using dynamic light scattering (DLS) on the SBF solution containing pAsp. The particles were primarily composed of precursors with an average diameter of ≈5.0 nm, as shown in Figure S2 in the Supporting Information. This was later confirmed using inductively coupled plasma optical emission spectroscopy (ICP-OES) to determine the levels of Ca and P. The average diameter of the complexes was found to increase with a higher initial concentration of PO_4^{3-} ions and as incubation time increased in m-SBF, as shown in **Figure 3**a. DLS measurements of the pAsp complexes at various $Ca^{2+}/[PO_4]^{3-}$ ratios showed average diameters of ≈15.1 and 14.6 nm at $Ca^{2+}/[PO_4]^{3-}$ ratios of 1/5 and 1/10, respectively. The diameters, respectively, increased to 32.1 and 35.9 nm for the 1/15 and 1/20 ratios immediately after introduction of pAsp into freshly prepared m-SBF solution. For a solution with a 1/5 $Ca^{2+}/[PO_4]^{3-}$ ratio, the average diameter was around 15.1 nm and slowly increased to 42.0 nm over 24 h of incubation. For 1/10 $Ca^{2+}/[PO_4]^{3-}$ ratio, the diameter was 14.6 nm which increased steadily to 56.3 nm over 12 h and 130.6 nm over 24 h. However, for higher $Ca^{2+}/[PO_4]^{3-}$ ratios, 1/15 and 1/20, the diameters of complexes abruptly increased to ≈129.0 and

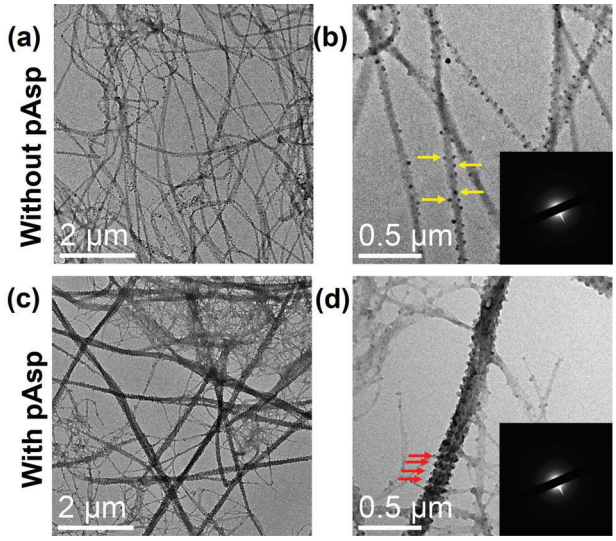

Figure 2. Bright-field TEM images with low- (left panels) and high-magnification (right panels) and corresponding SAED patterns, as insets, of the self-assembled Col-PDA fibrils in the presence of c,d) pAsp and a,b) with no pAsp. With no pAsp, a) low and b) high magnification of TEM images show the discrete contrast of fibrils as bright regions. The particles were found as nodules randomly attached along the fibrils (marked with yellow arrows). The contrast of TEM images shows clear differences in contrast due to the denser minerals from precursors on fibrils. With pAsp, the c) low magnification and d) high magnification of TEM images show that more particles are attached on fibrils creating darker contrast compared to specimens with no pAsp. Low-magnification images show preferential mineral deposition in gap zones, as evidenced by the pronounced banding pattern (marked with red arrows). All SAED patterns confirmed that the dark contrast particles are amorphous, as shown in (b) and (d) as insets.

145.0 nm within 12 h and then to ≈136.0 and 165.0 nm in 24 h, respectively, but at a slower speed as a saturation stage was likely achieved. The charge potential of pAsp complex was further investigated using zeta potential measurements (Table S1, Supporting Information). At a 1/5 $Ca^{2+}/[PO_4]^{3-}$ ratio, the zeta potential was around -9 ± 2 mV at the initial stage of incubation. These values were more negative with increased PO_4^{3-}concentrations, as shown in Figure 3b. The pAsp complexes therefore tended to become more negatively charged at various rates with increased incubation time. In Figure 3b, the high PO_4^{3-} concentration resulted in faster development of more negatively charged species over time. Saturation is achieved at ≈−30 to −36 mV. The saturation behavior of surface charges could be due to the limited number of PO_4^{3-} ions that can bind to a single pAsp-Ca complex. The concentrations of Ca and P measured by ICP-OES are presented in Table S2 in the Supporting Information and corresponding plots as a function of incubation time are shown in FigureS3 in the Supporting Information. At early stages, complexes containing Ca and P ions evolved into amorphous globular nanoobjects. Ca ions were accommodated in pAsp faster than phosphate ions as the zeta potential became more negative with increasing levels of P ions and incubation time.

The pAsp complexes in m-SBF with $Ca^{2+}/[PO_4]^{3-}$ ratios of 1/5 to 1/20 were expected to consist of Ca and P ions. Electrostatic repulsions are thought to cause pAsp molecules to arrange into a randomly twisted stretched chain structure. Ca ions can chemically interact with two carboxyl groups from the same pAsp molecule, which was also confirmed using energy-dispersive X-ray spectroscopy (EDS) elemental mapping, as shown in Figure S4 in the Supporting Information and **Figure 4**. The dark-field image in Figure 4a shows the bright contrast of Ca and P with more scattering for elements heavier than C from the supporting film in a TEM grid. The particles binding on fibrils are the coils of collapsed pAsp molecules with Ca-concentrated clusters.[40,48] The corresponding EDS spectrum of Figure 4 is shown in Figure S5 in the Supporting Information. From the early stage of mineralization in Figure S4 in the Supporting Information (1.5 to 3 h), the detected P signal is relatively weaker. pAsp complexes contain more Ca ions as indicated by their zeta potential (Figure 3b). The distribution of Ca and P along fibrils is confirmed by EDS mapping, as shown in Figure 4b,c, respectively, indicating pAsp complexes had infiltrated into the fibrils after 6 h. It also indicated that the Ca content is higher than that of P. The initial $Ca^{2+}/[PO_4]^{3-}$ ratio has an effect on the precursor chemistry, which is shown to be related to the size and surface charge potential of the pAsp complex. Various initial $Ca^{2+}/[PO_4]^{3-}$ ratios induce different Ca and P bonding geometries. It was reported by Hoeher et al. that a $Ca^{2+}/[PO_4]^{3-}$ ratio of 1/5 produced monodentate bonding geometries, while the ratio of 5/1 primarily resulted in bidentate structures. As the ratios of $Ca^{2+}/[PO_4]^{3-}$ were increased from 1/5 to 5/1, the initial monodentate geometry directly transformed into HAp as a result of a faster pathway to form HAp, while some or all of the initial bidentate formed a brushite phase.[31] It can be hypothesized that the mineralization pathway involves pAsp complexes directly transforming into HAp with increased incubation time, as Ca and P ions form a monodentate Ca-P geometry.

Mineralization was first verified by X-ray diffraction (XRD) at various $[PO_4]^{3-}$ concentrations. XRD data as a function of incubation time and different $Ca^{2+}/[PO_4]^{3-}$ ratios are presented in **Figure 5**. An XRD pattern showed the absence of HAp for 6 to 48 h, with the low concentration ratio of $Ca^{2+}/[PO_4]^{3-}$, 1/5, as shown in Figure 5a. At a concentration ratio of 1/10, in Figure 5b, the peaks at 31°–33° correspond to the interplanar spacing of (211), (112), and (300) planes in crystalline HAp (ICDD 09–0432). They started to appear at 6 h. This was also observed with higher concentrations of P, at $Ca^{2+}/[PO_4]^{3-}$ ratios of 1/15, and 1/20, as can be seen in Figure 5c,d, respectively. However, the peak intensity of the 1/10 $Ca^{2+}/[PO_4]^{3-}$ ratio after 6 h is relatively smaller than those of the 1/15 and 1/20 ratios. This resulted from differences in the amount of HAp formation. The presence of crystalline HAp, shown as broad peaks agreed well with the report by Li et al. for real bone apatite crystals from a rabbit femur.[49] The mineralization results using Col-PDA with $Ca^{2+}/[PO_4]^{3-}$ ratios of 1/10, 1/15, and 1/20 are shown in Figure 5b–d, respectively. They also show similar broad diffracted peaks of a rabbit femur. All of patterns showed broad peaks in the 2θ range of 10°–35°, which is a typical pattern of Col-I. The characteristic pattern of Col-I also can be detected from Col-PDA in Figure 5e as a before-mineralization reference. At the early stage of mineralization, 6 h, all XRD patterns revealed broad peaks between 10° and 35°, indicating the banding characteristics of Col-I before disappearing with increasing HAp formation during intrafibrillar mineralization.

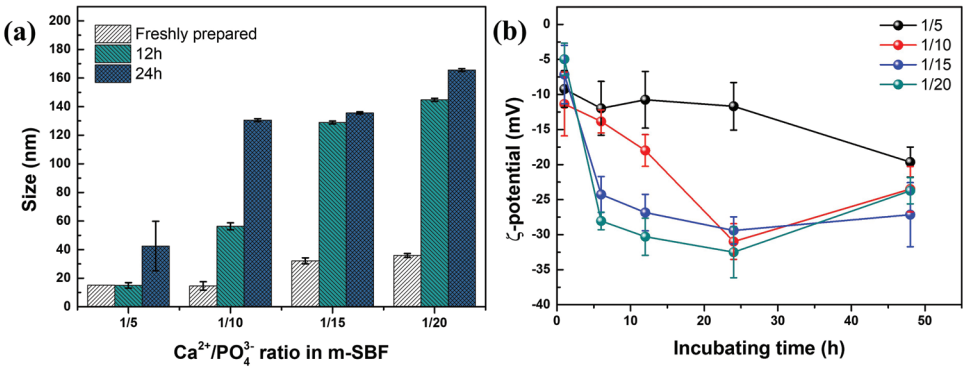

Figure 3. DLS spectra and zeta potential analysis of precursors in the m-SBF solution. a) DLS spectra show the increased diameters of complexes with greater $[PO_4]^{3-}$ concentrations and incubation times. b) Zeta potential measurements show that the surface charges of complexes are close to neutral at the initial stages and became negative with greater incubation time. Zeta potential decreased slowly in the 1/5 $Ca^{2+}/[PO_4]^{3-}$ ratio and abruptly showed more negatively charged surfaces within 12 h for 1/15 and 1/20 $Ca^{2+}/[PO_4]^{3-}$ ratios.

FTIR analysis was also performed to determine the chemical composition of mineralized Col-PDA fibrils. These results are shown in Figure S6 in the Supporting Information. The mineralized Col-PDA fibrils revealed the presence of phosphate and carbonate bands (at 1190–976, 961, and 660–520 and 873 cm^{-1}, respectively) and the peaks of amide bands like those found in Col-I fibrils. For the 1/5 $Ca^{2+}/[PO_4]^{3-}$ ratio (Figure S6a, Supporting Information), there was a small peak intensity for the phosphate band at 48 h, shown in blue, while it was absent at 6, 12 and 24 h, shown as black, red, and green lines, respectively. For the 1/10 $Ca^{2+}/[PO_4]^{3-}$ ratio, the spectra showed no phosphate band at 6 h, but it started to form after 12 h. Clear bands were observed at 24 and 48 h, as shown in Figure S6b in the Supporting Information. For high concentration ratios of $Ca^{2+}/[PO_4]^{3-}$, 1/15 and 1/20 (Figure S6c,d, Supporting Information), the spectra clearly showed signs of HAp mineralization after only 6 h. Mineralized Col-PDA fibrils have a chemical makeup similar to that of bone tissue. Therefore, the mineralized Col-PDA fibrils produced in m-SBF can be considered biomimetic intrafibrillar mineralization. The typical spectral features of HAp are clearly revealed for 1/15 and 1/20 $Ca^{2+}/[PO_4]^{3-}$ ratios. The main phosphate band at 1000–1100 cm^{-1} corresponds to the asymmetric stretching mode of PO_4^{3-} groups (v_1PO_4), while the 1/5 and 1/10 $Ca^{2+}/[PO_4]^{3-}$ ratios did not show this band, as can be seen in **Figure 6**a. After 12 h, in Figure 6b, the spectra were similar to those at 6 h, as the phosphate band was mainly detected for the 1/15 and 1/20 $Ca^{2+}/[PO_4]^{3-}$ ratios. When incubation time was increased to 24 and 48 h (Figure 6c,d), the FTIR spectra showed a phosphate band for the 1/10 $Ca^{2+}/[PO_4]^{3-}$ ratio specimen after 24 h and for the 1/5 ratio $Ca^{2+}/[PO_4]^{3-}$ specimen after 48 h. The band was sharper in the samples prepared with the higher concentrations of $[PO_4]^{3-}$, which resulted from more favorable conditions for HAp mineralization.

Intrafibrillar mineralization was directly observed using TEM. These images are shown in **Figures 7** and **8** as a function of incubation time and concentration ratios of $Ca^{2+}/[PO_4]^{3-}$. TEM images reveal bundles of needle-like mineral structures, i.e., crystalline HAp, oriented along the fibrils. The lowest concentration of $[PO_4]^{3-}$, the 1/1 $Ca^{2+}/[PO_4]^{3-}$ ratio, showed no sign of mineralization even after 7 days, as shown in Figure 7a and in the SAED results presented as an inset of this figure. After increasing the $Ca^{2+}/[PO_4]^{3-}$ ratio to 1/5, the first sign of crystallization was detected as a partly dark contrast along the fibrils in bright-field TEM image after 24 h in Figure 7b. This was also confirmed by the corresponding SAED ring pattern of crystalline HAp in the inset of this figure. After increasing the $Ca^{2+}/[PO_4]^{3-}$ ratio to 1/10, TEM images in both low and high magnification, Figure 8a, show less dense electron contrast regions in fibrils due to an amorphous phase. This is confirmed in the corresponding SAED patterns given as insets to these figures. After 8 h, the low-magnification TEM image in Figure 8b indicates darker contrast along fibrils with more Ca and P ions infiltrating into

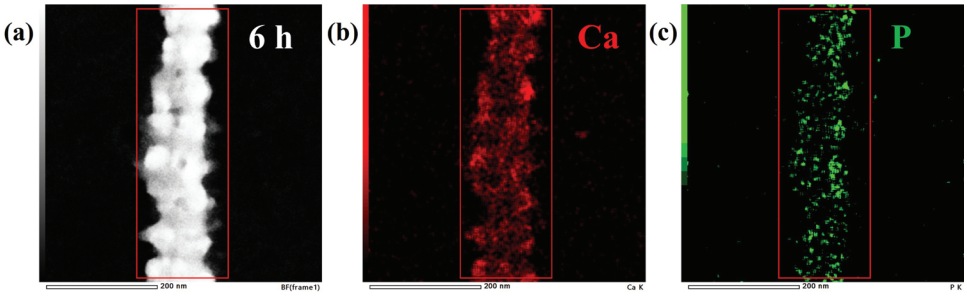

Figure 4. The early mineralization stage of Col-PDA fibrils with a $Ca^{2+}/[PO_4]^{3-}$ ratio of 1/15 in an m-SBF solution for 6 h. a) Dark-field images of TEM showed regions with heavier elements containing Ca and P with bright contrast. b) The detected Ca signal was found mostly along the Col-PDA fibril, c) while P was detected as lower levels.

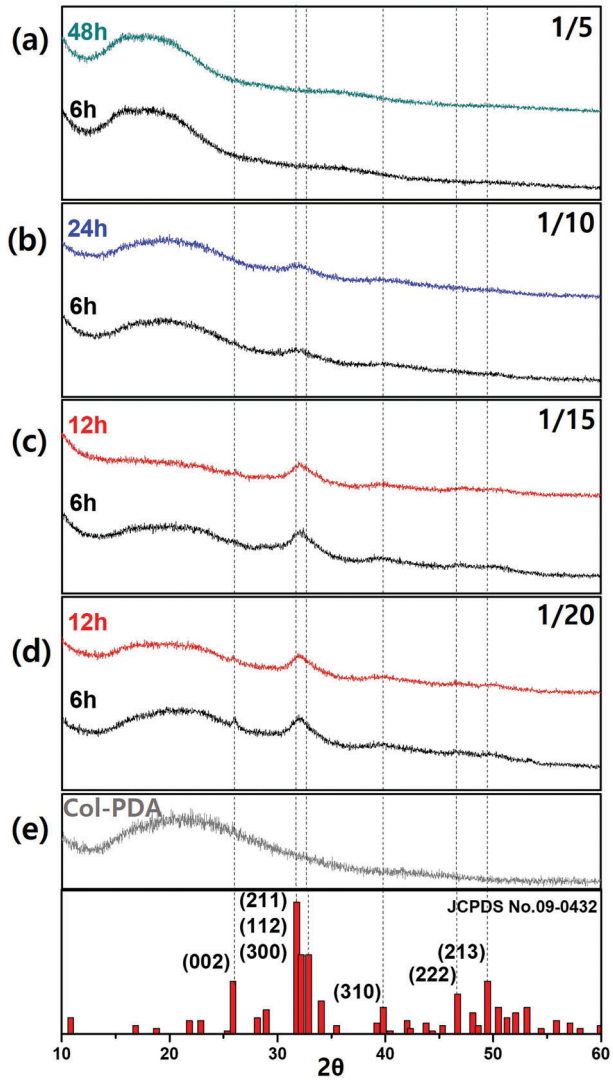

Figure 5. XRD patterns of Col-PDA fibrils mineralized in m-SBF solutions with $Ca^{2+}/[PO_4]^{3-}$ ratios of a) 1/5, b) 1/10, c) 1/15, d) 1/20, and e) Col-PDA before mineralization with JCPDS of HAp as a reference. The merged diffraction lines (28–29° and 31–33°) from HAp are found after 6 h of mineralization from 1/10, 1/15, and 1/20 $Ca^{2+}/[PO_4]^{3-}$ ratios with faster development in peak intensity of the 1/15, 1/20 ratios, presented as red lines for 12 h. This is compared with a 1/10 $Ca^{2+}/[PO_4]^{3-}$ ratio given as a blue line for 24 h. For the 1/5 ratio, there was no sign of HAp formation even after 48 h of mineralization.

fibrils. This is also seen in the high-magnification TEM image in Figure 8b as a diffuse ring in the SAED pattern, indicating the transformation of an amorphous phase was initiated. Intrafibrillar mineralization was incomplete after 10 h. Partial intrafibrillar mineralization of the bundles, with needle-like HAp as the dark contrast, was observed in low-magnification TEM image (Figure 8c). The diffraction pattern of the (002) plane was also found in the SAED data in the inset of this figure, indicating the *c*-axis-oriented HAP crystallites formed along fibrils. Additionally, the (211), (112), and (300) diffraction planes were also detected, but these three planes are close to each other, producing thicker and apparently continuous diffuse rings of lattice spacings, *d*, of 2.814, 2.778, and 2.720 Å, respectively (inset of Figure 8c, right panel). After increasing the $Ca^{2+}/[PO_4]^{3-}$ concentration ratio to 1/15 for 6 h of mineralization (Figure 8d), an amorphous phase was still predominant, but began to transform into a crystalline phase, as confirmed by the formation of a diffused ring SAED pattern similar to a $Ca^{2+}/[PO_4]^{3-}$ ratio of 1/10 after 8 h. Intrafibrillar mineralization with a $Ca^{2+}/[PO_4]^{3-}$ ratio of 1/15 can be observed after 8 h (Figure 8e) and 10 h (Figure 8f), respectively. HAp formation after both incubation times was confirmed by SAED patterns showing the diffraction patterns of the (002) and (211), (112), and (300) diffraction planes. TEM image from a specimen with a $Ca^{2+}/[PO_4]^{3-}$ ratio of 1/20 showed the dark contrast of almost fully mineralized HAp. This was confirmed by the SAED pattern in the inset of Figure 7c. The band patterns with different contrasts are shown in the high-magnification TEM images in Figure 8c,e,f, which is caused by Ca and P ion infiltration into the fibrils. The apparent increased cross-banding corresponds to the *d*-spacing of collagen molecules within the fibrils. This is due to the spatial effects of a 40 nm gap with 27 nm overlap regions. As a result, intrafibrillar mineralization occurs mainly in the 40 nm gap region, creating darker contrast.[50]

The kinetics of intrafibrillar mineralization was investigated by determining a mineralization degree (m.d) as a function of incubation time. The m.d was calculated as the ratio of the mineralized portion of fibrils to that of the whole fibrils. In **Figure 9**, the m.d was calculated using ImageJ, as explained briefly in the Experimental Section. For each analysis, at least five TEM images were analyzed to calculate the mean value and standard deviation of the m.d.[51,52] From low concentration of $[PO_4]^{3-}$, where the $Ca^{2+}/[PO_4]^{3-}$ ratio is 1/1, mineralization of fibrils could not be obtained even after 7 days, as shown in Figures 9 and 7a. For a $Ca^{2+}/[PO_4]^{3-}$ ratio of 1/5, a small degree of localized intrafibrillar mineralization was observed, with an m.d of 0.04 ± 0.09. Full mineralization for the $Ca^{2+}/[PO_4]^{3-}$ ratio of 1/5 can be observed after 48 h with an m.d of 1, which indicates that all fibrils are completely mineralized. For a $Ca^{2+}/[PO_4]^{3-}$ ratio of 1/10, a 0.47 ± 0.32 m.d was obtained after 8 h. Then, it increased to 0.79 ± 0.06 after 10 h, with full mineralization after 12 h. Increasing the $Ca^{2+}/[PO_4]^{3-}$ ratio from 1/5 to 1/10 induced a drastically changed rate constant of mineralization. Then, for a 1/15 $Ca^{2+}/[PO_4]^{3-}$ ratio, the m.d after 6 h was 0.44 ± 0.16, 0.51 ± 0.07 after 8 h, and 0.74 ± 0.05 after 10 h. This specimen was fully mineralized, m.d = 1, after 12 h. Interestingly, the different m.d values obtained from TEM image analysis of the 1/10 and 1/15 $Ca^{2+}/[PO_4]^{3-}$ ratios share almost the same rate constant, as shown in the overlapping red and blue lines in Figure 9. For the 1/20 $Ca^{2+}/[PO_4]^{3-}$ ratio, the rate constant of mineralization increased to 0.54 ± 0.14 at 3 h and 0.78±0.03 after 6 h. Full mineralization was achieved within 3 h. Higher rate constants were observed with increased $[PO_4]^{3-}$ concentrations in the m-SBF. The negatively charged pAsp complexes were likely to be more favorable attracted to the positively charged regions of fibrils (known as a-band), inducing an infiltration process at the early stage of mineralization. The faster development of pAsp-complex consisting of Ca and P ions was found by increasing the concentration of PO_4^{3-}. Since the pAsp-complexes with the higher concentration of $[PO_4]^{3-}$ could act as an optimal nucleus in the gap, subsequently, the intrafibrillar mineralization also

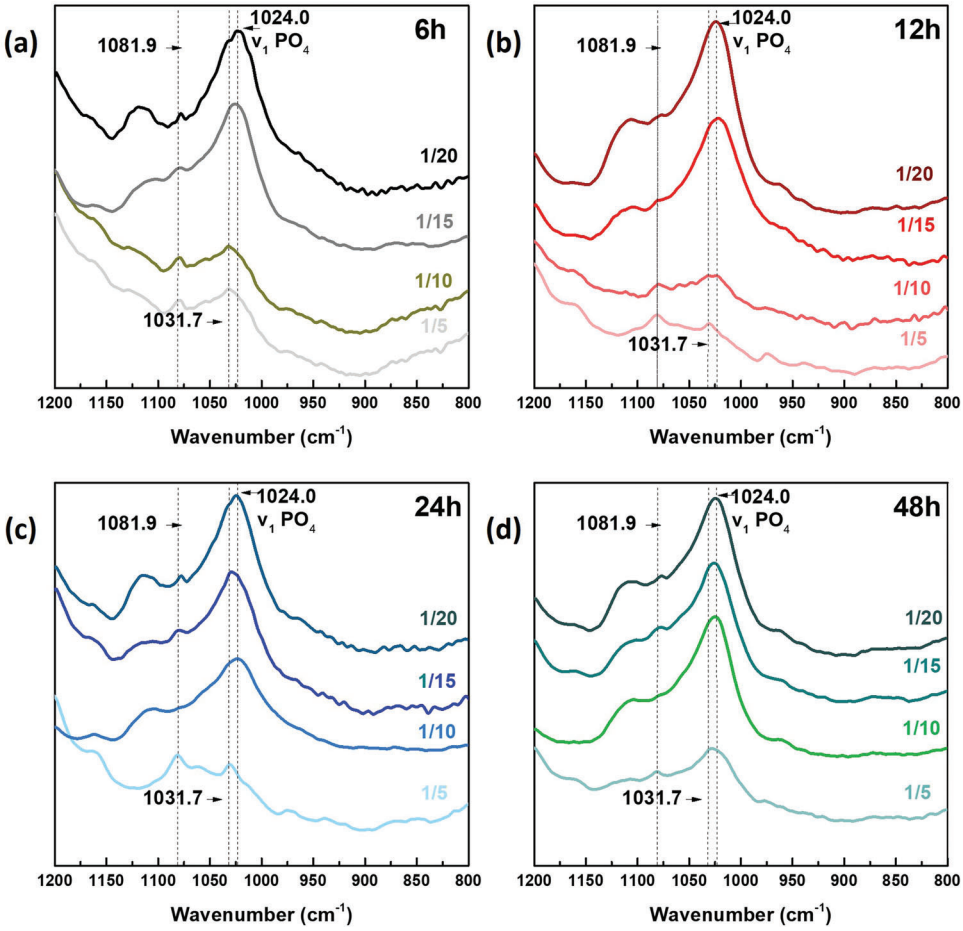

Figure 6. FTIR spectra of Col-PDA fibrils mineralized at various $Ca^{2+}/[PO_4]^{3-}$ ratios, 1/5, 1/10, 1/15, and 1/20 for a) 6, b) 12, c) 24, and d) 48 h, respectively. The spectra show intensity differences among the phosphate bands at 1190–976 cm^{-1} that occurred at shorter mineralization times for higher $[PO_4]^3$ concentrations, $Ca^{2+}/[PO_4]^{3-}$ ratios of 1/15 and 1/20 compared with a 1/5 ratio. The 1082 cm^{-1} wavenumber is ascribed to the antisymmetric stretching mode on Col-PDA fibrils and 1032 cm^{-1} results from the v_3 PO_4 stretching modes of HAp.

observed in the faster kinetics. HAp crystallization occurs within the confined space of the gap region, where it could reduce the energy barrier.[53–55] Together with the optimum pAsp complexes in the confined gap can even further be reduced the energy barrier, thereby enabling intrafibrillar mineralization at such a low temperature (37 °C). The intrafibrillar mineralization rate, as m.d, of HAp was demonstrated as a linear dependence on time in this study. At high PO_4^{3-} concentrations, the rate of mineralization was drastically increased compared to lower PO_4^{3-} levels, both with a linear dependency. As diffusion tends to be negligible, the rate-controlling reaction is likely interfacial. Linear growth of intrafibrillar HAp mineralization is consistent with interface-controlled crystallization inside the confined space of the fibrils with the minimal energy barrier of mineralization.

To better understand the biocompatibility, we examined the proliferation of a cell line using the 3-(4,5-dimethylthiazol-2-yl)−2,5-diphenyltetrazolium bromide (MTT) assay. Cytotoxicity and proliferation of the MC3T3-E1 preosteoblast cell line were tested. For this experiment, Col-PDA fibrils were deposited on a nontreated plate as a Col-PDA plate. The MC3T3-E1 preosteoblast cells were cultured in three ways, on a Col-PDA plate, tissue culture-treated (TC) plate, and bare glass to compare their proliferation. The seeded cells were incubated in a 6-well plates. The proliferation of MC3T3-E1 preosteoblast cells increased when they were cultured on a TC plate and Col-PDA plates. Proliferation of the MC3T3-E1 preosteoblast cells cultured on Col-PDA fibrils showed absorbance measured at a 570 nm wavelength increased to 0.673 ± 0.023, while those cultured on a TC-plate and bare-glass were, respectively, 0.566 ± 0.255 and 0.424 ± 0.037 after 24 h of incubation (Figure S7, Supporting Information). It is clearly seen that Col-PDA fibrils supported the highest proliferation among the three substrates. Increased cell proliferations could contribute to a collagen- and PDA-rich environment that acts as the ECM for the cells. Also, Ca and P ions in fibrils possibly interacted with the cells, resulting in active growth.[56] Collagen and PDA were tested as biomineralized membranes with biocompatible properties, have a high stress strength, and can promote MC3T3-E1 cell proliferation.[57] Although the MTT assay confirmed that Col-PDA fibrils on cell culture plate were nontoxic and enhanced proliferation of the MC3T3-E1 preosteoblast cell line, the viability of the cells cultured on Col-PDA fibril-coated surfaces was tested. The cytotoxicity to MC3T3-E1 cells cultured

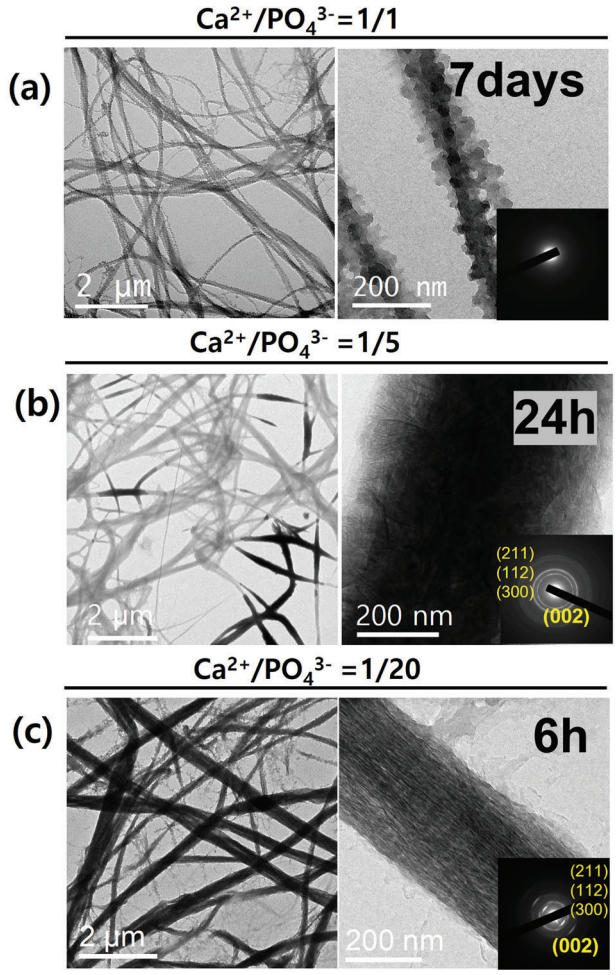

Figure 7. Bright-field TEM images and corresponding SAED patterns of mineralized Col-PDA fibrils in different m-SBF solutions a) $Ca^{2+}/[PO_4]^{3-}$ = 1/1 incubated for 7 days, b) $Ca^{2+}/[PO_4]^{3-}$ = 1/5 incubated for 24 h, and c) $Ca^{2+}/[PO_4]^{3-}$ = 1/20 incubated for 6 h.

on different plates was determined using a live/dead cell viability assay after 24 and 48 h. The TC-plates were used as positive controls and nontreated glass substrate used as the negative control for comparison with Col-PDA plates. This method employs two fluorescent dyes to distinguish live and dead cells. Live cells produce green fluorescence by converting calcein AM to calcein, while an ethidium homodimer-1 (EthD-1) enters damaged cell membranes, binds to nucleic acids, and fluoresces red. The cell growth in Figure S8 in the Supporting Information shows that the Col-PDA fibril coated plate was not only nontoxic but also biologically active, offering promising potential as a scaffold material.

3. Conclusions

Col-PDA fibrils were self-assembled in the presence of pAsp in an SBF solution. The mineralization of Col-PDA was enhanced by decreasing the $Ca^{2+}/[PO_4]^{3-}$ ratio of m-SBF solutions. At high PO_4^{3-} concentrations, the rate of mineralization was drastically increased compared to lower PO_4^{3-} levels with a linear dependency. At the early stages of mineralization, before crystallization, complex formation of Ca, P ions, and pAsp liquid precursors is dominant. The mineral complexes travel to collagen fibrils and deliver/infiltrate into them. The complexes were possibly infiltrated into the confined space of the collagen gap, a region that is rich in functional groups (as carboxyl and amine groups) for nucleation and growth of HAp. After full mineralization, the (002) diffraction plane of HAp was observed as an arc-shaped reflection that is an indicative of the *c*-axis-oriented HAp crystallites along the longitudinal axis of the Col-I fibrils, which is similar to natural bone tissue. The mineralization rate revealed in this work shows an m.d of a constant growth rate behavior. Intrafibrillar growth of HAp demonstrated a linear dependence on time. Additionally, PO_4^{3-} concentration has an effect on the mineralization rate, with higher concentrations leading to faster kinetics. The correlation between a linear growth rate and an interface-controlled interaction was demonstrated. Additionally, the influence of PO_4^{3-} was found to affect both nucleation and growth, depending on the PO_4^{3-} concentration. The 1/10 and 1/15 $Ca^{2+}/[PO_4]^{3-}$ ratio specimens exhibited analogous rate constants but showed different m.d values for the same incubation time. This phenomenon was suggested as an effect of the different numbers of HAp nuclei after the $Ca^{2+}/[PO_4]^{3-}$ ratio was increased to 1/15. The results presented in this work could serve as a guideline to better understand the mechanism of HAp mineralization in collagen fibrils, which may provide approaches to effective material design for efficient bone tissue engineering.

4. Experimental Section

Materials: Poly(L-aspartic acid sodium salt) (pAsp, 27 kDa) was purchased from ALAMANDA Polymers (Huntsville, AL, USA). Acid soluble Col-I from rat tails was purchased from Corning (Bedford, MA, USA). Calcium chloride ($CaCl_2$), disodium phosphate (Na_2HPO_4), sodium chloride (NaCl), dopamine hydrochloride (DA, $C_8H_{11}NO_2{\cdot}HCl$), glycine ($C_2H_5NO_2$), potassium chloride (KCl), sodium azide (NaN_3) were all obtained from Sigma-Aldrich (St. Louis, MO, USA). Tris-HCl (1 M, pH 8.5) was purchased from CureBio (Seoul, South Korea). Deionized water was autoclaved prior to use.

Self-Assembly of Collagen Fibrils: An SBF solution was prepared using the self-assembly process of Kokuba and Takadama.[41] The self-assembly process of fibrils was initiated with dopamine polymerization. A 10×10^{-6} M dopamine solution was prepared with a 10×10^{-3} M Tris-HCl buffer at pH 8.5, for use as a solvent. The weight ratios of Col-I and PDA were set to 5:16 as an optimized condition from previous study, which determined the best conditions for the collagen fibrosis and mineralization processes. After mixing the prepared PDA and SBF solutions, Col-I was immediately added to above prepared solution to make at a 50 μg mL^{-1} concentration of Col-I and incubated at 37 °C for 12 h.

Mineralization of Collagen with Polydopamine: m-SBF was prepared separately from calcium and phosphate stock solutions. The calcium stock solution was prepared by dissolving 3.34×10^{-3} M of $CaCl_2$ in DI water. The phosphate stock solution was made as a series of different phosphate concentrations, prepared individually by dissolving 1.5×10^{-3}, 9.5×10^{-3}, 19×10^{-3}, 28.5×10^{-3}, and 38×10^{-3} M of Na_2HPO_4 and 300×10^{-3} M of NaCl in DI water. The 1.5×10^{-3}, 9.5×10^{-3}, 19×10^{-3}, 28.5×10^{-3}, and 38×10^{-3} M Na_2HPO_4 solutions with a constant 3.34×10^{-3} M concentration of $CaCl_2$ refer to the $Ca^{2+}/[PO_4]^{3-}$ concentration ratios, respectively, of 1/1, 1/5, 1/10, 1/15, and 1/20 m-SBF solutions. A 0.37 M pAsp solution was mixed with the prepared calcium stock solution for a final pAsp concentration of 0.566 mg mL^{-1}. After that, the phosphate stock solution was mixed with the pAsp/calcium stock solution in the same

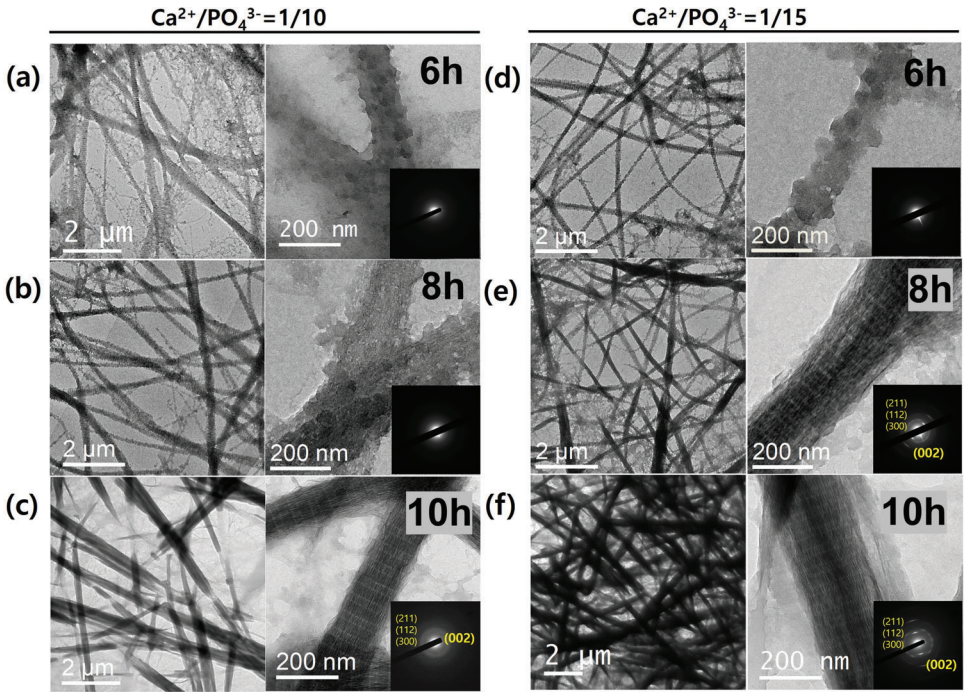

Figure 8. Bright-field TEM images and corresponding SAED patterns of mineralized Col-PDA fibrils. The self-assembled Col-PDA fibrils were incubated in m-SBF with $Ca^{2+}/[PO_4]^{3-}$ = 1/10 for a) 6, b) 8, c) 10 h, and $Ca^{2+}/[PO_4]^{3-}$ = 1/15 for d) 6, e) 8, and f) 10 h. The mineralization for $Ca^{2+}/[PO_4]^{3-}$ = 1/10 for 6 h showed no mineralization in agreement with its SAED patterns (a). b) Intrafibrillar mineralization started to form at 8 h for $Ca^{2+}/[PO_4]^{3-}$ = 1/10 and d) 6 h for $Ca^{2+}/[PO_4]^{3-}$ = 1/15, confirmed by the diffuse ring formation in the SAED patterns. c) Col-PDA fibrils from $Ca^{2+}/[PO_4]^{3-}$ = 1/10 m-SBF for 10 h and e) 1/15 for 8 h were partially mineralized. f) Intrafibrillar mineralization of Col-PDA fibrils in $Ca^{2+}/[PO_4]^{3-}$ = 1/15 for 10 h, at 37 °C was fully mineralized and the corresponding SAED pattern matched that of crystalline HAp.

volume ratio as the calcium and phosphate stock solutions. Then, 5% NaN_3 was added to the mineralization solution and mixed quickly to retard bacterial growth. All m-SBF samples were sealed to control the evaporation rate and incubated at a constant temperature of 37 °C for a designated time. The mineralized solutions were freshly changed at every 24 h.

Material Properties of Mineralized Collagen Fibrils: XRD and FTIR spectroscopy analyses were performed to observe changes in the material properties of Col-PDA and mineralized fibrils. The self-assembled fibrils for these measurements were prepared using the methods described in the *Self-assembly of Collagen Fibrils* section above at the same concentration with a larger final solution volume of 50 mL to obtain enough fibrils for characterization. After incubation for 12 h, SBF was removed from all samples by centrifugation at 4000 rpm for 15 min and washed three times using autoclaved DI water.

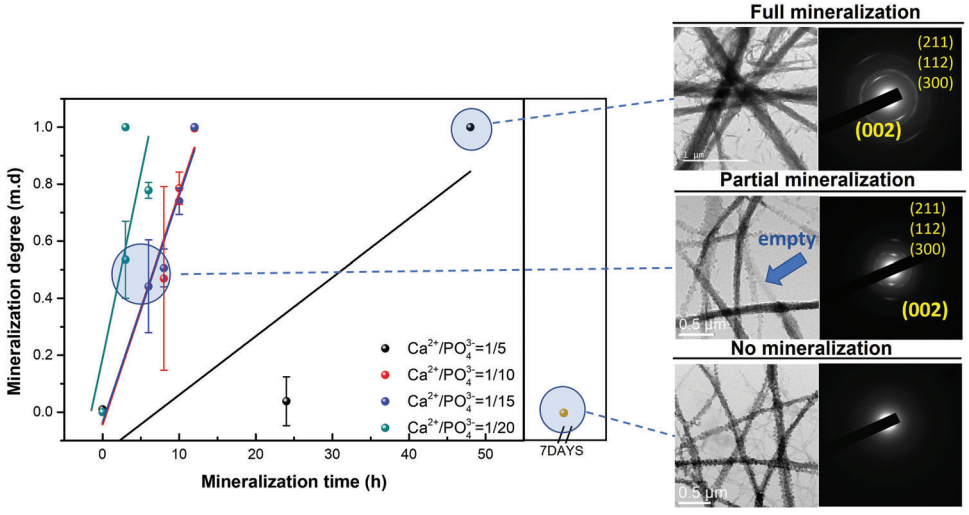

Figure 9. Degree of mineralization of Col-PDA fibrils calculated from the mineralized regions in TEM images (right panel) of each stage of mineralization. The upper TEM image shows full mineralization, middle panel shows partial mineralization stage with some areas not yet mineralized (blue arrow), the bottom panel shows no mineralization.

Mineralization Degree Calculation: Higher contrast regions in TEM images were mainly due to differences in electron density of the materials being analyzed. Lower contrast areas were selected. The mineral phase, with its relatively heavy atoms (Ca and P), appeared significantly darker compared to the nonmineralized portion, which contained lighter atoms (C, H, N). The background particles were characterized using the method of Smeets et al.[51] The particles were selected by thresholding pixels with intensities lower than $\bar{I} - 2\sigma$, where $\bar{I}$ is the mean density and σ is a standard deviation of density in the TEM images. A typical TEM image contains different features due to carbon film (background), nonmineralized collagen fibrils, and mineralized collagen fibrils. A histogram of each TEM image was split into three Gaussian distributions (Figure S9, Supporting Information). By choosing thresholding pixels with intensities lower than $\bar{I} - 2\sigma$ for each Gaussian distribution, the regions of mineralized collagen fibrils, nonmineralized collagen fibrils, and the background could be identified. Then, ImageJ was used to obtain a summary of pixel intensities from the mineralized portion (S1) and nonmineralized collagen fibrils (S2), allowing calculation of the mineralization degree (m.d.) as $m.d = \frac{S1}{S1+S2}$.[51,52]

Cell Culture: MC3T3-E1 cells were cultured in an alpha minimum essential medium supplemented with 10% fetal bovine serum and 1% penicillin-streptomycin (pen-strep). Cells were grown in a humidified atmosphere with 5% CO_2 at 37 °C. The culture medium was changed every other day. The seeding density of the cells on all substrates was 2.0×10^4 cells per $cm^{2.}$

Proliferation of Cells: Col-PDA was used for the proliferation experiment to compare with a negative control, bare glass substrate, and a positive control, tissue culture treated plate (TC-plate). MC3T3-E1 cells with a seeding density 2×10^4 per cm^2 were cultured on Col-PDA fibrils, positive control, and negative control substrates for 24 and 48 h. A filtered solution of 5 mg mL^{-1} MTT in DI water was mixed with a serum-free medium (1:9 vol %). It was added following removal of the cell culture media after 24 and 48 h. It was incubated at 37 °C for 4 h. Cells that were actively respiring were able to convert the water-soluble MTT into a purple formazan that was insoluble. The MTT solution was replaced with dimethyl sulfoxide for lysis and dissolution of the formed formazan followed by incubation at 37 °C for 10 min. A spectrophotometer was used to record the 540 nm absorbance of the samples. The proliferation was calculated by subtracting the intensity of the cell-free samples from that of the cell line samples.

Live/Dead Assay: MC3T3-E1 with a seeding density 2×10^4 cells per cm^2 of plate were cultured and incubated for 24 and 48 h on the bare glass, Col-PDA plates, and TC plates using 6-well plates. A LIVE/DEAD viability/cytotoxicity kit for mammalian cells (Thermo Fisher) was used for this experiment. The assay solution consisted of 20 µL of EthD-1 added to 10 mL of phosphate-buffered saline (PBS), followed by addition of 5 µL of calcein AM. The cell culturing media in the samples were removed and specimens were washed twice with PBS, followed by treatment with the assay solution for 30 min in the dark. An inverted microscope (Leica) was used to image the live and dead cells. Green fluorescence (calcein, excitation (Ex)/emission (Em) = ≈494/517 nm) indicated live cells, while red fluorescence (ethidium/homodimer, Ex/Em = ≈528/617 nm) indicated dead cells. After this step, the live/dead imaging was revealed as the dead cells appear as a red color when exposed to a light source with a wavelength of ≈528/617 nm, while the live cells appear as green fluorescence when exposed to a light source with a wavelength of ≈494/517 nm.

Supporting Information

Supporting Information is available from the Wiley Online Library or from the author.

Conflict of Interest

The authors declare no conflict of interest.

Data Availability Statement

The data that support the findings of this study are available on request from the corresponding author. The data are not publicly available due to privacy or ethical restrictions.

Keywords

collagen, crystallization kinetics, hydroxyapatite, interface control, intrafibrillar mineralization

Received: May 9, 2023
Revised: June 13, 2023
Published online:

[1] R. P. Mecham, *Curr. Protoc. Cell Biol.* **2012**, *57*, 10.11.11.
[2] C. Frantz, K. M. Stewart, V. M. Weaver, *J. Cell Sci.* **2010**, *123*, 4195.
[3] B. Yue, *J. Glaucoma* **2014**, *23*, S20.
[4] M. Mizuno, R. Fujisawa, Y. Kuboki, *J. Cell. Physiol.* **2000**, *184*, 207.
[5] Y. Li, Y. Liu, R. Li, H. Bai, Z. Zhu, L. Zhu, C. Zhu, Z. Che, H. Liu, J. Wang, *Mater. Des.* **2021**, *210*, 110049.
[6] A. K. Nair, A. Gautieri, S.-W. Chang, M. J. Buehler, *Nat. Commun.* **2013**, *4*, 1724.
[7] A. K. Nair, A. Gautieri, M. J. Buehler, *Biomacromolecules* **2014**, *15*, 2494.
[8] J. Kinney, S. Habelitz, S. Marshall, G. Marshall, *J. Dent. Res.* **2003**, *82*, 957.
[9] U. G. Wegst, H. Bai, E. Saiz, A. P. Tomsia, R. O. Ritchie, *Nat. Mater.* **2015**, *14*, 23.
[10] Y. Liu, D. Luo, T. Wang, *Small* **2016**, *12*, 4611.
[11] S. Kuttappan, D. Mathew, M. B. Nair, *Int. J. Biol. Macromol.* **2016**, *93*, 1390.
[12] Z. Li, T. Du, C. Ruan, X. Niu, *Bioact. Mater.* **2021**, *6*, 1491.
[13] A. L. Boskey, *Biomaterials Science: An Introduction to Materials in Medicine*, 3rd ed. (Eds: B. Ratner, A. Hoffman, F. Schoen, J. Lemons), Elsevier, New York **2013**, pp. 151–161.
[14] S. Mondal, U. Pal, A. Dey, *Ceram. Int.* **2016**, *42*, 18338.
[15] D. Kim, B. Lee, S. Thomopoulos, Y.-S. Jun, *Nat. Commun.* **2018**, *9*, 962.
[16] Y. Liu, S. Thomopoulos, C. Chen, V. Birman, M. J. Buehler, G. M. Genin, *J. R. Soc., Interface* **2014**, *11*, 20130835.
[17] S. Wu, Y. Chen, X. Guo, Y. Wu, *Mater. Chem. Front.* **2021**, *5*, 7071.
[18] B. M. Oosterlaken, M. P. Vena, G. de With, *Adv. Mater.* **2021**, *33*, 2004418.
[19] D. Zhang, X. Wu, J. Chen, K. Lin, *Bioact. Mater.* **2018**, *3*, 129.
[20] Y. Liu, Y.-K. Kim, L. Dai, N. Li, S. O. Khan, D. H. Pashley, F. R. Tay, *Biomaterials* **2011**, *32*, 1291.
[21] U. Amornkitbamrung, Y. In, Z. Wang, J. Song, S. H. Oh, M.-H. Hong, H. Shin, *ACS Omega* **2022**, *7*, 4821.
[22] Y. Xu, F. Nudelman, E. D. Eren, M. J. Wirix, B. Cantaert, W. H. Nijhuis, D. Hermida-Merino, G. Portale, P. H. Bomans, C. Ottmann, *Nat. Commun.* **2020**, *11*, 5068.
[23] F. Nudelman, A. J. Lausch, N. A. Sommerdijk, E. D. Sone, *J. Struct. Biol.* **2013**, *183*, 258.
[24] L.-N. Niu, S. E. Jee, K. Jiao, L. Tonggu, M. Li, L. Wang, Y.-D. Yang, J.-H. Bian, L. Breschi, S. S. Jang, *Nat. Mater.* **2017**, *16*, 370.
[25] L. Fisher, D. Torchia, B. Fohr, M. Young, N. Fedarko, *Biochem. Biophys. Res. Commun.* **2001**, *280*, 460.
[26] M.-H. Hong, J. H. Lee, H. S. Jung, H. Shin, H. Shin, *Biomater. Res.* **2022**, *26*, 42.
[27] B. D. Quan, E. D. Sone, *J. R. Soc., Interface* **2018**, *15*, 20180269.

[28] Y. Qi, Z. Ye, A. Fok, B. N. Holmes, M. Espanol, M.-P. Ginebra, C. Aparicio, *ACS Biomater. Sci. Eng.* **2018**, *4*, 2758.
[29] L. Gu, Y. Kim, Y. Liu, H. Ryou, C. Wimmer, L. Dai, D. Arola, S. W. Looney, D. H. Pashley, F. Tay, *J. Dent. Res.* **2011**, *90*, 82.
[30] Q. Zhang, Y. Liu, B.-D. Gou, L. Zheng, Y.-X. Gao, T.-L. Zhang, *RSC Adv.* **2016**, *6*, 102710.
[31] A. J. Hoeher, S. T. Mergelsberg, O. J. Borkiewicz, F. M. Michel, *Cryst. Growth Des.* **2021**, *21*, 3736.
[32] L. M. Epasto, T. Georges, A. Selimovic´, J.-M. Guigner, T. Azaïs, D. Kurzbach, *Anal. Chem.* **2021**, *93*, 10204.
[33] B. Cantaert, E. Beniash, F. C. Meldrum, *J. Mater. Chem. B* **2013**, *1*, 6586.
[34] D. Toroian, J. E. Lim, P. A. Price, *J. Biol. Chem.* **2007**, *282*, 22437.
[35] H. Adelnia, H. D. Tran, P. J. Little, I. Blakey, H. T. Ta, *ACS Biomater. Sci. Eng.* **2021**, *7*, 2083.
[36] F. Nudelman, K. Pieterse, A. George, P. H. Bomans, H. Friedrich, L. J. Brylka, P. A. Hilbers, G. de With, N. A. Sommerdijk, *Nat. Mater.* **2010**, *9*, 1004.
[37] F. Nudelman, P. H. Bomans, A. George, N. A. Sommerdijk, *Faraday Discuss.* **2012**, *159*, 357.
[38] L. Yu, M. Wei, *Int. J. Mol. Sci.* **2021**, *22*, 944.
[39] F. Hang, H. S. Gupta, A. H. Barber, *J. R. Soc., Interface* **2014**, *11*, 20130993.
[40] Z. Zhou, L. Zhang, J. Li, Y. Shi, Z. Wu, H. Zheng, Z. Wang, W. Zhao, H. Pan, Q. Wang, *Nanoscale* **2021**, *13*, 953.
[41] T. Kokubo, H. Takadama, *Biomaterials* **2006**, *27*, 2907.
[42] J. Venugopal, S. Low, A. T. Choon, T. Sampath Kumar, S. Ramakrishna, *J. Mater. Sci.: Mater. Med.* **2008**, *19*, 2039.
[43] J. Kong, S. Yu, *Acta Biochim. Biophys. Sin.* **2007**, *39*, 549.
[44] M. J. Baker, J. Trevisan, P. Bassan, R. Bhargava, H. J. Butler, K. M. Dorling, P. R. Fielden, S. W. Fogarty, N. J. Fullwood, K. A. Heys, *Nat. Protoc.* **2014**, *9*, 1771.
[45] H. Yang, S. Yang, J. Kong, A. Dong, S. Yu, *Nat. Protoc.* **2015**, *10*, 382.
[46] A. Dey, P. H. Bomans, F. A. Müller, J. Will, P. M. Frederik, G. de With, N. A. Sommerdijk, *Nat. Mater.* **2010**, *9*, 1010.
[47] D. Gebauer, H. Cölfen, *Nano Today* **2011**, *6*, 564.
[48] E. Colaço, D. Brouri, C. Méthivier, L. Valentin, F. Oudet, K. El Kirat, C. Guibert, J. Landoulsi, *J. Colloid Interface Sci.* **2020**, *565*, 43.
[49] X. Li, Q. Zou, H. Chen, W. Li, *Sci. Adv.* **2019**, *5*, eaay6484.
[50] U. Hansen, D. F. Holmes, P. Bruckner, P. N. Bishop, *PLoS One* **2020**, *15*, e0234672.
[51] P. J. Smeets, A. R. Finney, W. J. Habraken, F. Nudelman, H. Friedrich, J. Laven, J. J. De Yoreo, P. M. Rodger, N. A. Sommerdijk, *Proc. Natl. Acad. Sci. U. S. A.* **2017**, *114*, E7882.
[52] C. Shao, R. Zhao, S. Jiang, S. Yao, Z. Wu, B. Jin, Y. Yang, H. Pan, R. Tang, *Adv. Mater.* **2018**, *30*, 1704876.
[53] D. Hentrich, M. Junginger, M. Bruns, H. G. Börner, J. Brandt, G. Brezesinski, A. Taubert, *CrystEngComm* **2015**, *17*, 6901.
[54] C. Carney, M. Fricke, S. Harry, H. Imai, R. Kniep, K. Sato, S. Sewell, P. Simon, D. Volkmer, D. Wright, *Biomineralization I: Crystallization and Self-Organization Process*, Springer, New York **2006**.
[55] W. Wöger, H. Müller-Krumbhaar, *J. Cryst. Growth* **1977**, *38*, 181.
[56] J. Wang, Y. Qu, C. Chen, J. Sun, H. Pan, C. Shao, R. Tang, X. Gu, *Mater. Sci. Eng., C* **2019**, *104*, 109959.
[57] X. Yu, J. Walsh, M. Wei, *RSC Adv.* **2014**, *4*, 7185.